JOURNAL OF PROPULSION AND POWER
Vol. 23, No. 6, November–December 2007

Flowfield Studies of a Diamond-Shaped Fuel Injector in a Supersonic Flow

Kan Kobayashi*
Japan Aerospace Exploration Agency, Kakuda, Miyagi 981-1525, Japan
Rodney D. W. Bowersox† and Ravichandra Srinivasan‡
Texas A&M University, College Station, Texas 77843
Campbell D. Carter §
U.S. Air Force Research Laboratory, Wright–Patterson Air Force Base, Ohio 45433
and
Kuang-Yu Hsu¶
Innovative Scientific Solutions, Inc., Dayton, Ohio 45440

DOI: 10.2514/1.30000

Studies were performed to characterize the flow structure and the mixing characteristics of a diamond-port flush-wall fuel injector at Mach 2.0 airflow. The goals were to examine the flow structure in the near-field region of the diamond- and circular-port injectors and to quantify the effects of igniter torch flow on the near-field flow structure with and without torch gas. Planar laser-induced fluorescence was used to document the flow trajectories and the injector-barrel shock shape for the injectors. For the inert mixing studies, the flow was seeded with a nitric-oxide-trace probe molecule, whereas for the reacting experiments, naturally occurring hydroxyl was used. The present experiments confirmed recent computation results that implied that under certain conditions, a diamond-shaped injector port could be tailored to improve mixing and produce an additional secondary flow structure with gasdynamic flame-holding potential. It was also shown that an igniter torch system could be incorporated without adversely affecting the tailored flow structure.

I. Introduction

COMBINED-CYCLE engines offer the potential for hypersonic propulsion over a wide range of flight Mach numbers. A rocket-based combined-cycle engine, for example, operates in ejector-jet mode, ramjet mode, scramjet mode, and then rocket mode as the flight Mach number increases. One of the key technological challenges has been attaining sufficient fuel–air mixing and stable flame holding during the ramjet/scramjet modes of operation. The scramjet mode is particularly difficult, because fuel and air residence times within the engine are of the order of milliseconds. Thus, improving mixing and flame holding are current research areas.

There are numerous fuel-injector concepts under consideration [1–3]. In the present work, the focus is on flush-wall injection through diamond-shaped orifices, as introduced by Tomioka et al. [4] and Bowersox et al. [5]. The flowfield structure for these injectors is fully described in [4–6]. Tomioka et al. [4] demonstrated that diamond-port injection produced better penetration than that with corresponding circular injectors. Moreover, far-field penetration was further enhanced by sweeping the injector in the streamwise direction. Additional increases were found by adding yaw. Bowersox et al. [5] examined near-field flow structure at Mach 5.0. When comparing circular- and diamond-port injectors, they found that in the near field, the circular-injector penetration was larger than that of all diamond ports tested. However, all of the diamond-port-injector penetrations exceeded that of the circular port when their correlation parameter exceeded about 2.0. Their pressure results confirmed weaker shocks and shorter standoff distances for the diamond port than those for the circular port.

Srinivasan and Bowersox [6] investigated the secondary flow structure associated with injection into a supersonic freestream using both Reynolds-averaged Navier–Stokes (RANS) and high-fidelity detached eddy simulation (DES) tools. These simulations provided evidence that in addition to weaker losses through the shock, the sharp leading-edge flow of the injector produced a pair of vortices that provide additional mixing. These vortices were called the leading-edge-mixing vortex pair. Also, through these simulations, they were able to use the injector-port geometry and injector-to-freestream static pressure ratio to tailor the secondary flow structure downstream of the injector. More specifically, they identified an opportunity within the design space to produce a trapped lateral vortex pair just downstream of the injector-barrel shock. The strength of the vortex pair was similar to that of the well-documented axial vortex pair [2] within the plume that is responsible for the far-field mixing. They denoted this new structure as the lateral counter-rotating vortex pair (LCVP), and they were able to show that the structure was closely coupled to the barrel shock shape. The tailored barrel shock and LCVP for case 6 from Srinivasan and Bowersox [6] are shown in Fig. 1. The streamlines that were entrained into the LCVP were found to be in the domain 10 times longer than those that were not, which suggested that the LCVP structure has the potential to act as a gasdynamic flame-holding device. The potential advantages of eliminating mechanical flame-holding devices (e.g., cavities [7] that cause significant losses and flow instabilities) provide the motivation for the present study.

The objective for the present study was to characterize the near-field flow structure and mixing of the Srinivasan and Bowersox [6] case 6 diamond injector. To accomplish this objective, a series of

Presented as Paper 5416 at the 43rd AIAA/ASME/SAE/ASEE Joint Propulsion Conference and Exhibit, Cincinnati, OH, 8–11 July 2007; received 24 January 2007; revision received 10 May 2007; accepted for publication 11 May 2007.

*Researcher, Combustion and Control Section, Combined Propulsion Research Group. Member AIAA.
†Associate Professor, Aerospace Engineering. Associate Fellow AIAA.
‡Postdoctoral Research Associate, Aerospace Engineering. Member AIAA.
§Senior Aerospace Engineer, Aerospace Propulsion Division. Associate Fellow AIAA.
¶Senior Engineer (Corporate Vice President). Associate Fellow AIAA.

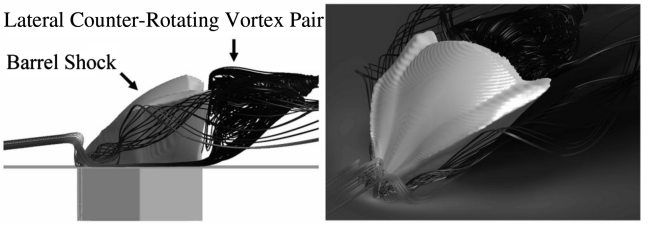

a) Side view **b) Perspective view**

Fig. 1 Tailored barrel shock and associated LCVP for case 6 in [6].

mixing and combustion tests were performed in the Mach 2.0 facility at Wright–Patterson Air Force Base. The goals of the tests were to 1) examine the flow structure in the near-field region of diamond- and circular-port injectors using advanced laser diagnostics and 2) quantify the effects of igniter torch flow on the near-field flow structure with and without torch gas.

A circular-port injector was included in the test matrix for comparison purposes. Planar laser-induced fluorescence (PLIF) was used to characterize the flowfields. For the nonreacting studies, the injector gas was air. The air was seeded with nitric oxide (NO) to serve as the PLIF probe molecule. For the reacting tests, the injector gas was ethylene (C_2H_4) and the naturally occurring hydroxyl radical (OH) reaction product was used as the PLIF probe molecule. The facility was operated at temperatures below those for autoignition. Hence, a combustion-gas-type torch igniter [8] with a mix of ethylene and oxygen was used. Complementary numerical simulations were performed for the present experiments to provide additional flow characterization.

II. Experimental Apparatus and Simulation Setup

A. Test Facility, Fuel Injector, and Torch Igniter

Both the nonreacting and reacting tests were conducted in the U.S. Air Force Research Laboratory's continuous-flow supersonic wind tunnel, described by Gruber and Nejad [9]. The flow condition and injector-port geometry were chosen to approximate case 6 in [6]. A two-dimensional converging–diverging Mach 2.0 nozzle section was used in this study. The nozzle-exit height and width were 127 and 152.4 mm, respectively. The total temperature of the airflow was fixed at 300 ± 5 K for the nonreacting tests (NO-PLIF diagnostics) and 589 ± 10 K for reacting tests (OH-PLIF diagnostics). The total pressure of the airflow was 207 ± 5 kPa for all tests. As a result, the mass flow rate of the freestream was 5.52 kg/s for nonreacting tests and 3.94 kg/s for reacting tests.

The test section was connected directly to the facility nozzle exit. There were five axial stations on the bottom wall of the test section for installing test blocks. The test block is shown in Fig. 2. The second station, which was located approximately 457 mm downstream of the nozzle exit, was used in this study. At this location, the boundary-layer thickness was estimated as 8 mm [9]. The test block had an insert that housed the fuel injector and torch injector(s). Various configurations of fuel injector and torch injector(s) could be tested by changing this insert. Shown in Figs. 3a and 3b are schematics of the inserts with a diamond injector that were used in this study. The insert was made of 17-4 precipitation-hardened stainless steel and was 12.7 mm thick, and graphite sheet gasket was used for sealing. The exit of a diamond injector had 15-deg semivertex angles and a 12.7-mm-long major axis, resulting in a cross-sectional area of 21.6 mm^2. This geometry was based on the findings in Srinivasan and Bowersox [6]. For comparison, an insert with a circular injector (shown in Fig. 3c) was also tested. The exit diameter of the circular injector was 5.25 mm, which had the same cross-sectional area as the diamond injector. To obtain relatively high discharge coefficients Cd, the flowpaths of the injectors were contained linear convergence regions, reducing the area to the injector port. The discharge coefficients were found to be 0.91 and 0.86 for the diamond and circular injectors, respectively.

As for the torch injector(s), two options were tested in this study: namely, a single-port torch (Fig. 3a) and a dual-port torch (Fig. 3b).

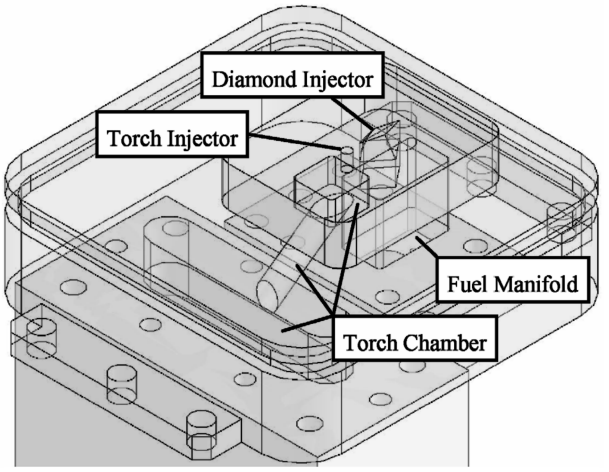

a) Perspective view

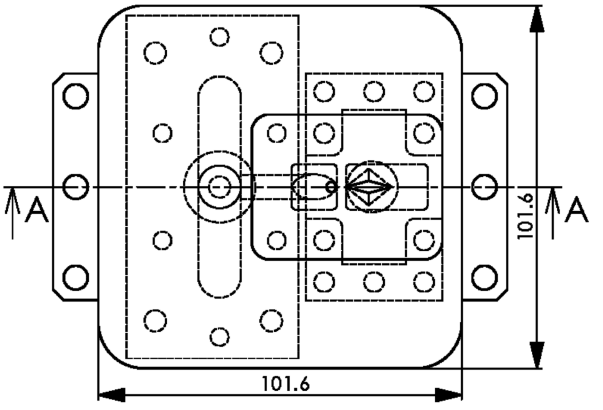

b) Top view

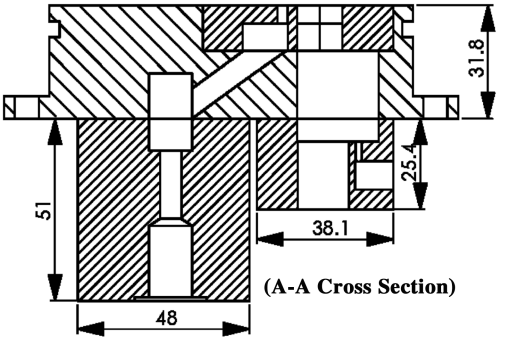

c) Cutting plane

Fig. 2 Schematic of the test block (dimensions in millimeters).

The diameters of the torch injectors were 2.87 mm for the single-port torch and 2.03 mm for the dual-port torch, resulting in the same total cross-sectional area of 6.48 mm^2 for both cases. The converging structure of the flowpath was not applied to the torch injector, because the depth of the injector was only 5.08 mm; a discharge coefficient of the torch injector was sufficiently high at 0.87 for the single-port torch, for example. There was a torch-gas manifold (which had a depth of 7.62 mm) below the torch injector, as shown in Figs. 2 and 3. Torch injection both upstream and downstream of the main injector was tested by rotating the test block by 180 deg.

The main body of the torch igniter was 96 mm long, 48 mm wide, and 49 mm thick and it was made of nickel. It has been used previously as a hydrogen/oxygen torch igniter for the hydrogen-fueled scramjet engine tests ([10], for example), and the basic torch performance was described in Kobayashi et al. [11]. For the present

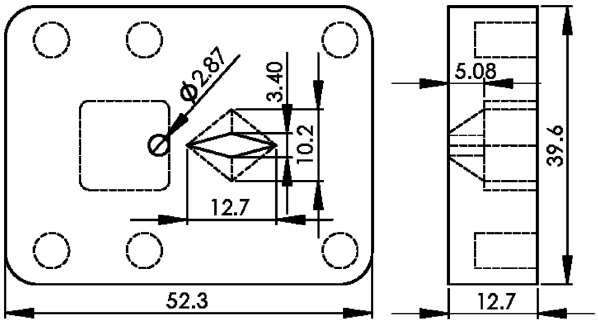

a) Diamond injector with single-port torch

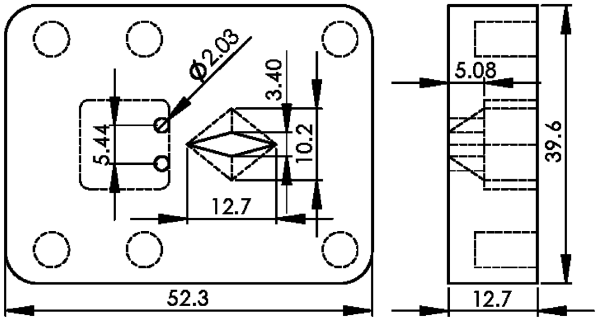

b) Diamond injector with dual-port torch

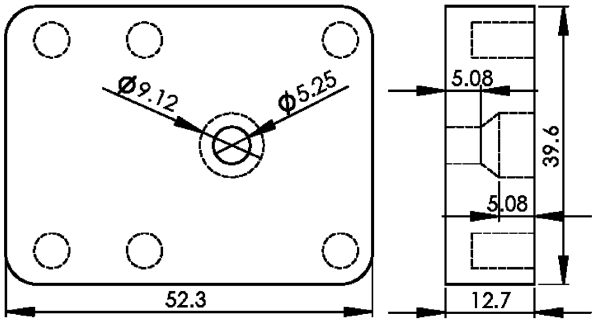

c) Circular injector without torch

Fig. 3 Schematics of the injector inserts (dimensions in millimeters).

tests, the igniter consisted of a spark-plug port, an ethylene port, an oxygen port, a chamber-pressure tap, and a combustion chamber. The chamber-pressure tap was also used as a nitrogen-purge port. Ethylene and oxygen were supplied into the chamber, each through a choked orifice to prevent flashback and to fix the flow rates. Note that the combination of the torch-injector diameter and choked-orifice diameters had to satisfy a certain relationship to ensure choking. In this study, the orifice diameters for ethylene and oxygen were 0.584 mm ($Cd = 0.77$) and 0.711 mm ($Cd = 0.92$), respectively. The mixture of ethylene/oxygen was ignited by a spark plug (NGK-BUR9EQ), and the combustion gas was supplied to the torch-gas manifold in the insert through the flowpath in the test block. For attaining torch ignition, the operation sequence was as follows. First, the spark plug was turned on. Second, torch oxygen flow was initiated. Third, after the torch chamber was filled with oxygen, the torch ethylene was started. In this study, fuel-rich [equivalence ratio (ER) of 2.0] combustion was tested to avoid oxidation in the torch and to provide additional fuel for reaction in the freestream to promote flame holding.

According to equilibrium calculations following [12], it was found that the excessive fuel for the fuel-rich condition existed as hydrogen. This was deemed preferable for ignition promotion in the test section, because reaction rates of hydrogen are higher than those of ethylene. For the case with an ER of 2.0 (chamber pressure of 600 kPa and mass flow rate of 1.8 g/s), 26% by volume of the torch-gas products were hydrogen. The torch gas was also a source of radicals: for this case, 7.76% by volume of the torch-gas products were radicals (O, H, and OH). The adiabatic combustion gas temperature was predicted to be 3200 K. The discharge coefficient of the torch injector (single-port torch) was 0.87, as previously mentioned. Thus, from the coefficient, measured mass flow rate, and measured torch chamber pressure, we estimated the actual temperature of the torch gas, including the heat loss. By using the actual temperature and adiabatic temperature, the thermal efficiency was estimated as approximately 50% in our experiments; that is, half of the combustion heat was lost to the torch body in the present configuration. As a result, the temperature, pressure, and net input power were estimated as 1750 K, 450 kPa, and 8 kW, respectively, for the torch considered here.

B. PLIF Diagnostics

Instantaneous measurements of the mixing and reacting flowfields were obtained using planar laser-induced fluorescence of NO and OH, respectively. In the NO-PLIF technique, a supply of air seeded with less than 500 ppm of nitric oxide was used as the injectant. The OH-PLIF technique relies on the presence of the hydroxyl radical in the reacting-flow experiments.

Schematics of optics configurations for NO- and OH-PLIF diagnostics are shown in Fig. 4a. For both NO- and OH-PLIF, a Lumonics Hyperdye dye laser was pumped with the second harmonic of an injection-seeded Spectra Physics Nd:YAG laser (GCR-170). The dye-laser output was frequency-doubled using an Inrad Autotraker 3. To generate the wavelength for NO excitation, a second Autotraker 3 was employed in which the doubled-dye beam was frequency-mixed with the residual infrared beam from the Nd:YAG. For NO excitation, the dye laser was set to a wavelength of 574 nm to produce frequency-mixed radiation at 226 nm to couple to the $R_1(8)$ transition of the $A^2\Sigma^+ - X^2\Pi$ (0,0) band. For OH excitation, the dye laser was tuned to 567 nm so that the frequency-doubled radiation matched the wavelength for the $Q_1(8)$ transition of the $A^2\Sigma^+ - X^2\Pi$ (1,0) band. In both cases, the resulting pump-beam-line width was approximately 0.1 cm^{-1}. To ensure good overlap of the laser and transition, a portion of the UV beam was split off and directed over a small reference flame (and then to a fast photodiode); a simple set of lenses collected and focused the resulting LIF onto the photocathode of a photomultiplier tube. This signal, along with the photodiode output, was continuously displayed on an oscilloscope, allowing minor adjustments to be made to the dye-laser wavelength to mitigate the effects of laboratory temperature changes.

The laser sheet was formed using a pair of fused silica lenses, a planoconcave cylindrical lens (using either a −50-mm or a −100-mm focal length), and a planoconvex spherical lens (1000-mm focal length). This arrangement resulted in a sheet height of about 75 mm (limited by the diameter of the turning mirrors). This sheet was directed either through the top fused silica window (wall) of the tunnel and viewed from the side, as shown in Fig. 4b, or across the span of the test section (through the side window) and viewed off-axis to the sheet normal, as shown in Fig. 4c. In the latter case, image blur was effectively mitigated by using a Scheimpflug mount, similar to what is done in stereo particle image velocimetry. The transmitting and receiving optical hardware were positioned on a traversing table, allowing remote positioning of the measurement volume at any desired station in the flowfield.

A Princeton Instruments Superblue PIMAX intensified CCD camera (512 × 512 pixel array) was used to detect the fluorescence; the pixels were binned 2 × 2 before readout so that the camera could achieve a 10 frame/s readout, thus matching the laser repetition rate. The camera gate was set to 100 ns, but the fluorescence pulse is only slightly longer than the laser pulse; the interrogation time is thus about 10 ns. Typically, 300 instantaneous NO-PLIF images were acquired (and then averaged afterward); for OH probing, 100 instantaneous images were used to produce each average image. The camera was fitted with a 45-mm $f1.8$ UV lens (Cerco), and Schott glass filters were used to block scattering at the laser wavelength. For OH-LIF detection, fluorescence from the A–X (0,0) and (1,1) bands was isolated using UG-5 and WG-305 filters; for NO-LIF detection, a

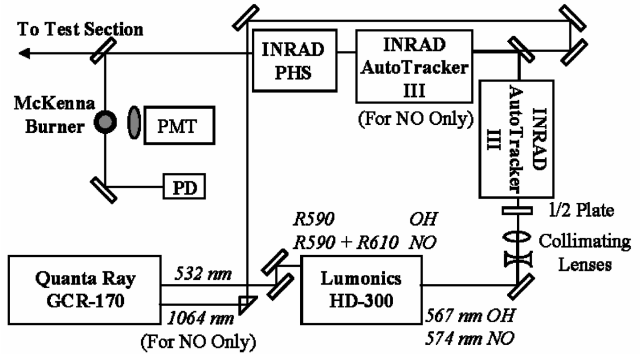

a) Optics configuration for NO- and OH-PLIF diagnostics

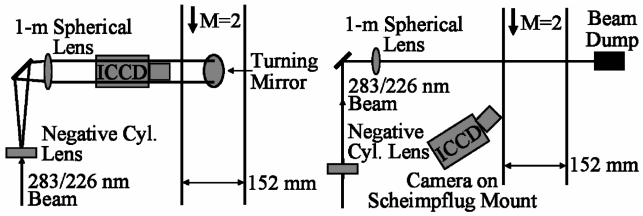

b) Optics configuration for side-view imaging

c) Optics configuration for spanwise-view imaging

Fig. 4 Schematics of optics configurations.

UG-5 filter blocked scattering at 226 nm [as well as fluorescence from the (0,0) band], and fluorescence was collected from the $(0, 1), (0, 2), (0, 3), \ldots, (0, n)$ bands. The LIF images were not corrected for variation in line broadening, electronic quenching, or ground-state population. However, the NO images were corrected for background laser scattering, camera-intensity offset, and nonuniform laser-sheet irradiance. All of the warped spanwise images due to camera alignment were also corrected for perspective distortion using a linear transformation constructed from images of a calibration card that consisted of an array of dots.

To generate the flat-field image for normalization of the NO images, the NO-laden N_2 was injected in the plenum upstream of the nozzle, whereas the tunnel was under vacuum conditions (but no compressor air was flowing); this provided a uniform concentration of NO that was well suited for image normalization. In some cases, multiple flat-field images were recorded; for the spanwise image set, for example, flat-field images (along with the background images) were collected at all three downstream locations. Note, however, that the laser-intensity distribution does vary somewhat over time, and thus the normalization approach is only approximate. Furthermore, window blemishes, either permanent or temporary, can lead to striations in the original images. Again, depending on the nature of the artifact, its effect on the PLIF image may or may not be completely removed through normalization. Because of this normalization step, the peak intensity within each image, as displayed, is close to unity (depending on the relative strength of NO fluorescence in the image of interest and the normalization image). For the OH images, however, no corrections were made, and the images are in terms of camera signal counts; note that the camera intensity offset is about 1800 counts. The preceding corrections were deemed sufficient to qualitatively document the plume structure.

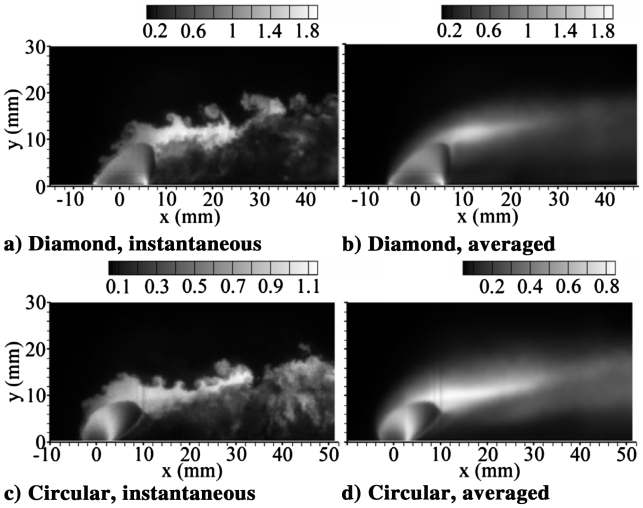

Fig. 5 Side view of NO-PLIF images (normalized intensity).

C. Numerical-Simulation Setup

Numerical simulations of the experimental setup were performed for the cases without torch injection and the results were compared. The simulations were performed using AeroSoft's GASP [13] flow solver. Structured grids were generated to encompass the domain of interest for the circular and diamond injectors. The losses in the port were accounted for by including the injector in the simulations. The inlet conditions for both simulations were identical and matched the experimentally measured boundary-layer thickness. Adiabatic no-slip conditions were used on the tunnel wall and the injector-port wall. Only half of the domain was used for the circular injector. A symmetry plane boundary condition was specified along the central axial plane of the tunnel. The full domain was used for the diamond-injector simulation. The total number of grid points for the circular- and diamond-injector simulations was approximately 2 and 4 million, respectively. Detailed grid and numerical convergence studies were performed, as described in [6]. The normalized numerical Euclidean norm residuals were all reduced by at least five orders of magnitude. Comparison of the present medium and fine grids showed that the secondary flow structure was captured with both grids, and the differences in the flow variables were less than 3% (in which the medium grid corresponded to the fine grid with every other point removed). Two different species were used to differentiate between the freestream and injector fluids; this helps in identifying the mole fractions in the plume. Inviscid fluxes were evaluated using the third-order MUSCL formulation of Roe's flux difference splitting [14] with Harten's entropy correction [15]. Turbulence was modeled using Wilcox's k-ω model [16].

III. Results and Discussion

A. Air-Injection Mixing Studies

1. *No-Torch Case*

In this section, the flow structure and mixing characteristics for air injection from both the diamond and circular ports are compared. The injector pressure ratio (defined as the injector-exit static pressure divided by the freestream static pressure) was fixed at 10.0 with the goal of producing the LCVP for the diamond injector [6]. Shown in Fig. 5 are side-view images along the tunnel centerline for the diamond and circular injectors. The freestream flow is from left to right. Figures 5a and 5c are from a single-laser pulse, which is essentially an instantaneous 10-ns snapshot. Figures 5b and 5d are ensemble averages composed of 300 laser pulses. The images are presented using a linear grayscale color map; the highest signal in each image corresponds to a display count level of 255, whereas the lowest value corresponds to zero. Note that the color map is provided to enable the reader to see how the fluorescence varied (and thus, in an approximate fashion, how the injectant concentration varied across the field of view), but not to enable comparison of individual images. The NO-seeded air from the injector is clearly visible in all of the images. These images clearly show the expected differences in the barrel shock shape between the diamond injector and circular injector, as discussed in [6]. Focusing on the diamond-port injector, the shape of the barrel shock is virtually identical to that shown in Fig. 1a. The vertical trailing edge of the barrel shock is clearly present and, as described in [6], this is a key ingredient in the formation of the LCVP. Note that these instantaneous images captured small vortex structures in the shear layer. However, the shape of the barrel shock in the average images was the same as that in the instantaneous

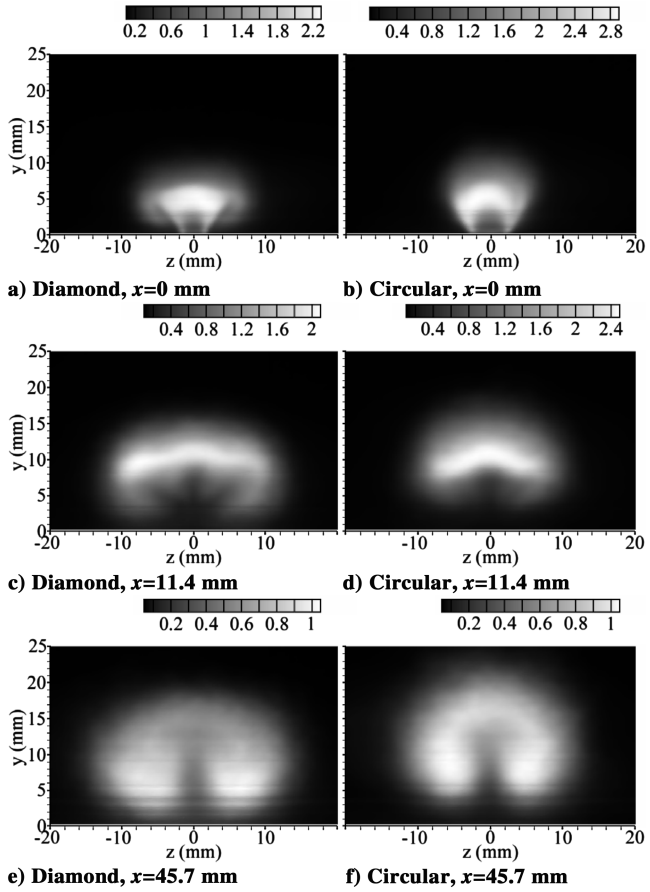

Fig. 6 Lateral view of NO-PLIF images (normalized intensity).

images, and thus the barrel shock was steady. This finding is consistent with the analyses of the time-accurate DES results in [17], in which it was found that the barrel shock and subsequent LCVP structures were nearly identical in both the instantaneous and time-averaged numerical results.

Shown in Figs. 6a and 6b are ensemble-averaged images of the flowfield on lateral planes centered on the injector [$x = 0$ mm ($x/d^* = 0$, where $d^* = 5.25$ mm)]. One clear difference between the two injectors is the shape of the injectant distribution. The diamond-injector-gas distribution is wider, with less penetration, than that for the circular-injector case (which, based on [5], was expected). Also discernible in Figs. 6a and 6b are the lateral edges of the barrel shocks. Again, the shapes closely match the numerical results in [6]. Of particular importance is the lateral V-shaped expansion of the diamond-port barrel shock, which was found to be an essential feature leading to the formation of the LCVP. The diamond-port images in Figs. 5b and 6a indicate that the overall three-dimensional shape of the barrel shock agrees with the predictions shown in Fig. 1.

A second clear difference between the diamond- and circular-injector flows (Figs. 6a and 6b) is an axial vortex for the diamond case. The cores of the vortices were located at approximately $y = 3$ mm and $z = \pm 5$ mm. Cores are also present in Fig. 6c for $x = 11.4$ mm at $y = 7$ mm and $z = \pm 7$ mm. A similar pair was not observed for the circular injector at these locations. It will be shown in the next section that these axial structures were also present in the numerical simulations. The potential advantage of these structures is the mixing enhancement, and this seems to result in the larger and apparently more diffuse diamond-injector plume at $x = 45.7$ mm ($x/d^* = 8.70$; Fig. 6e) than that with the circular plume at the same axial location (Fig. 6f). The simulations described in the next section support these experimental results.

Focusing on the $x = 11.4$ mm ($x/d^* = 2.17$) images in Figs. 6c and 6d, it was noticed that the overall shape of the NO signature was significantly different for the two injectors. The injector gas for both cases was concentrated, as indicated by the bright region of NO, in the upper layer of the plume. For the diamond injector, the plume was highly elongated in the lateral direction, which is consistent with reported axis switching [18]. A pronounced three-leafed-rose-shaped dark region was noticed below this region. The two outer petals correspond to the vortex pair mentioned earlier. The dark regions in Fig. 6c indicate an absence (or small amount) of NO. Thus, the pronged region was occupied mainly by freestream gas. The three-pronged structure was not apparent in the circular-injector plume. Instead, the plume appeared to take on the expected crescent-moon shape. Further downstream at $x = 45.7$ mm (Figs. 6e and 6f), the expected far-field cardioidal shape was seen for both injectors, which indicated the dominance of the counter-rotating vortex pair. The shape of the circular-injector plume in Fig. 6f is in good agreement with the planar Rayleigh/Mie scattering result from [18] (case CA at $x/d^* = 8$, pressure ratio of 11.8, and $M = 2.0$).

2. *Numerical Simulations for the No-Torch Case*

To better understand the flow structure around the injector, a RANS-based numerical simulation was performed under the same flow conditions as in the experiments. For these simulations, the injectant was air, as was the case in the present set of experiments. Shown in Figs. 7a and 7b are distributions of the injectant mole fraction in the x–y plane at $z = 0$ mm (the tunnel centerline) for diamond and circular injectors, corresponding to Figs. 5b and 5d, respectively, for the experiments. The plume penetration for the diamond injector was lower than that for the circular injector, showing a good agreement with the experimental results. Velocity-magnitude distributions in the same plane are shown in Figs. 7c and 7d for the flow region just around the barrel shock. The differences in barrel shock shape for the two injectors were clearly seen, in which the shapes qualitatively agreed with those observed in the experiments in Fig. 5. For the diamond injector, a relatively low-speed region was observed just behind the barrel shock, and the streamline distributions in Fig. 7e show that this region corresponds to the LCVP. For the circular injector, the lateral vortices and corresponding low-speed region were not observed. From Figs. 7a and 7e, the predicted injectant mole fraction in the LCVP was 70–90% in the upper (smaller) vortex region and 50–70% in the lower (larger) vortex region. For the ethylene/air mixture, the stoichiometric fuel mole fraction was 6.54% (19.62% O_2 and 73.84% N_2 for air), which suggested that the mixture in the LCVP was extremely fuel-rich for the conditions tested.

Lateral views of injectant distributions from the simulations are shown in Fig. 8. These images correspond to the experimental images in Fig. 6. Overall, the size, shape, and location of the injectant plume at all three locations for both diamond and circular injectors were qualitatively correct in the simulations, compared with the experimental data. The predicted trends in terms of width and height of the plume agreed well with the experimental results: namely, a narrower and taller plume was obtained for the circular injector.

The V-shaped cross section of the diamond-injector-barrel shock was seen at $x = 0$ mm ($x/d^* = 0$) (Fig. 8a) as observed in Fig. 6a. The predicted circular-injector-barrel shock shape was also very similar to that in the experimental data. The axial vortices seen in the experimental data were also seen in simulations at this location. The predicted location of the cores, $y = 3$ mm and $z = \pm 5$ mm, was in good agreement with the data. The structures were not predicted for the circular injector, which also agrees with the experimental findings.

The diamond-injector three-leafed-rose and elongated bright regions observed in the experiments at $x = 11.4$ mm ($x/d^* = 2.17$) (Fig. 6c) were captured in the numerical simulations (Fig. 8c). The two outer petals of the rose feature were verified to be the axial vortices described in the experimental data. The predicted locations of the vortices were $y = 6$ mm and $z = \pm 8$ mm, which is in excellent agreement with the experiment. From Fig. 7e , it was found that the predicted location of the LCVP was at $x = 8$–12 mm, with the center near 10 mm. The transverse extent was between $y = 2$ mm and 10 mm. The width of the LCVP was found to be very similar to

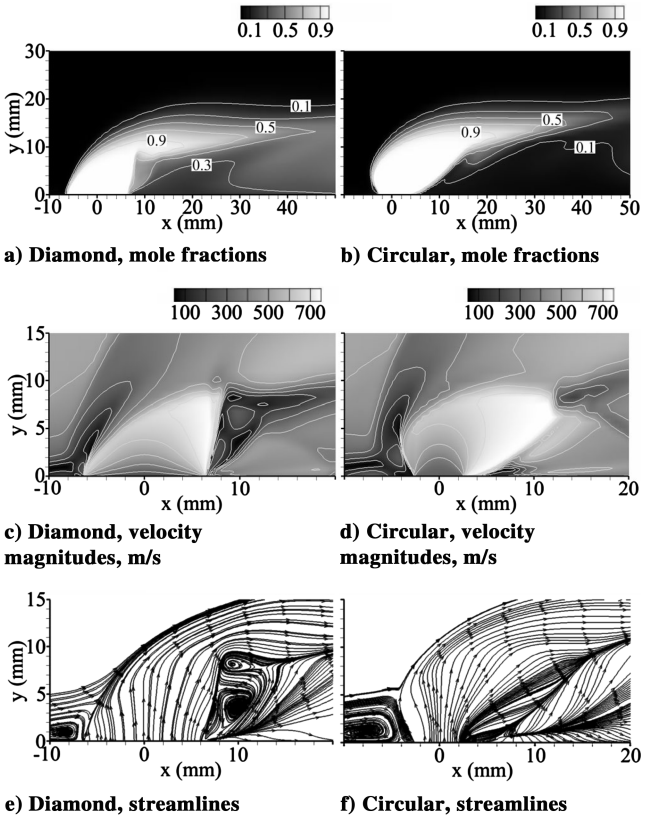

Fig. 7 Predicted flowfield in the *x*–*y* plane (RANS).

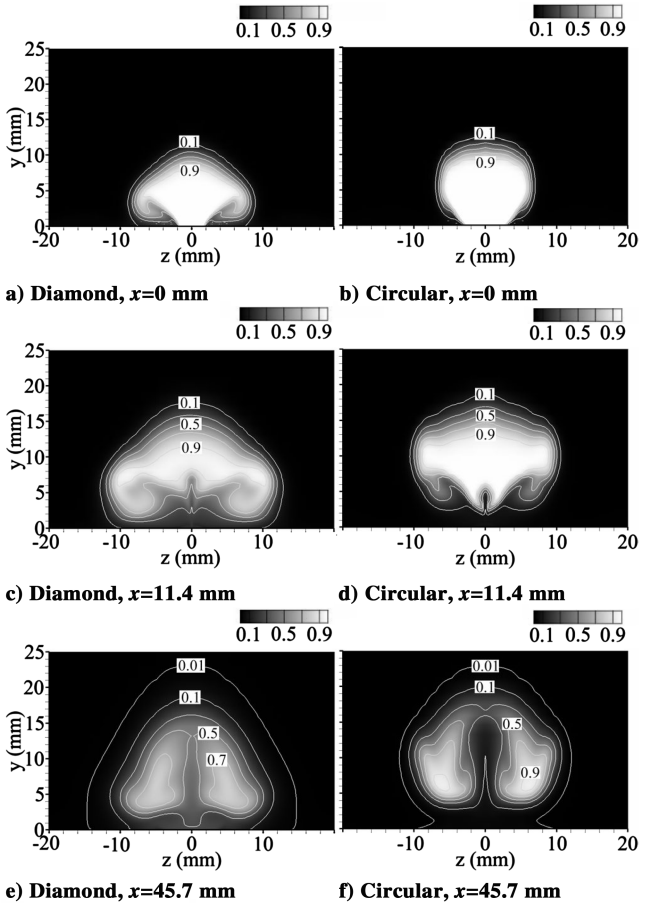

Fig. 8 Predicted mole fractions in the *y*–*z* plane (RANS).

that of the barrel shock. Thus, the center region of the three-leafed-rose structure in Fig. 8c corresponds to the LCVP, and the center-region in Fig. 6c provides experimental evidence for the presence of the LCVP.

The experimental data implied better mixing for the diamond injector at the last measurement station (Figs. 6e and 6f). The numerical simulations (Figs. 8e and 8f) also showed improved mixing for the diamond injector at this station. The peak concentration for the diamond injector was 81% and for the circular case it was 94%. The outer contours are not visible with the choice of grayscale levels in the numerical results. Hence, a 1.0% demarcation line was added to better define the plume edge.

3. Upstream-Torch Case

As mentioned in the experimental apparatus section, the injector blocks were fitted with igniter-gas ports, both upstream and downstream of the primary injector. The ports were used in the present mixing studies to inject the NO probe molecule into the primary crossflow. Thus, a series of tests was performed on the diamond injector to 1) examine the entrainment of the upstream boundary-layer flow into the downstream region and 2) characterize the effects of the torch injection on the overall flow structure. Air was injected through the torch ports at a pressure ratio (defined as the torch-exit static pressure divided by the freestream static pressure) of 4.0.

Presented in Fig. 9 are average images for the combined injector and torch flow for both the single-port torch (Figs. 9a and 9c) and the dual-port torch (Figs. 9b and 9d). Two sets of images for each flow condition are shown. In Figs. 9a and 9b, the primary-injector flow was seeded with NO, and in Figs. 9c and 9d, the torch flow was seeded with NO. In the case of the single-port torch (Figs. 9a and 9c), the leading edge of the barrel shock appears to have been truncated, and the penetration of the barrel shock was higher than in the no-torch case, which is expected due to the shielding effect of the torch flow on the primary injector. The tunnel center region of the barrel shock appeared to be unaffected by the dual-port torch. This is partially explained by noting that the total flow rate of the torch gas for both the single-port- and dual-port torches was the same, thus flow rate per port for the dual-port torch injector was half that of the single-port torch. Therefore, the disturbance to the flow was distributed more and thus less noticeable.

The torch-gas distributions in Figs. 9c and 9d demonstrated that most of the torch gas moved around the sides of the barrel shock and was then subsequently entrained in the wake region behind the barrel shock; this is consistent with the streamlines shown in Fig. 1b. The

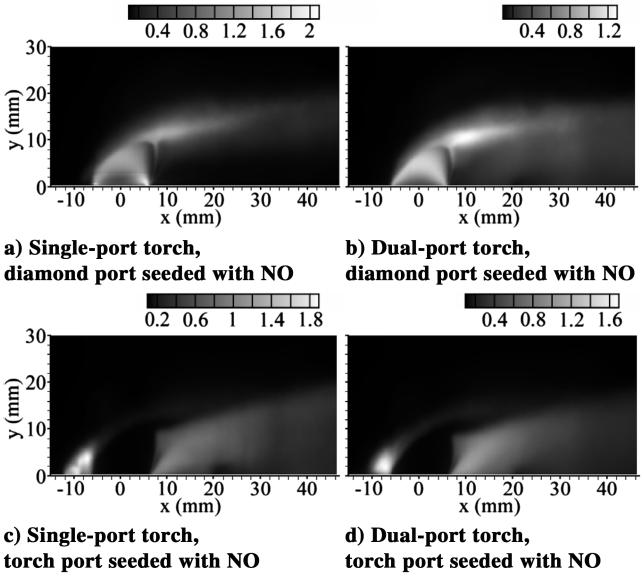

Fig. 9 Side view of NO-PLIF images (normalized intensity) with upstream-torch port injection.

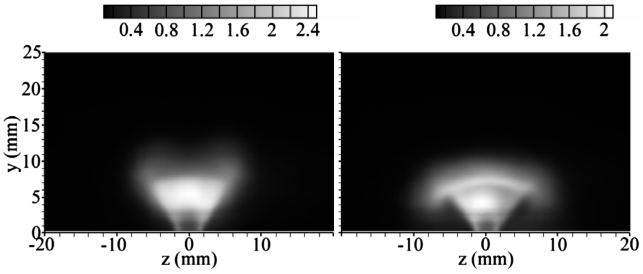

a) Single-port torch, diamond port seeded with NO

b) Dual-port torch, diamond port seeded with NO

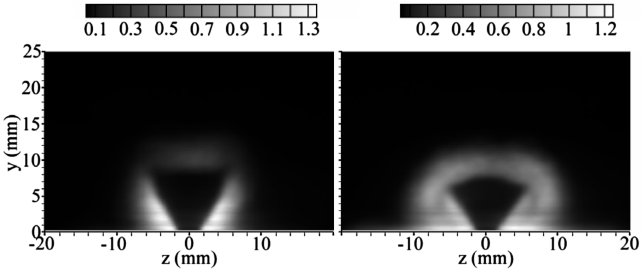

c) Single-port torch, torch port seeded with NO

d) Dual-port torch, torch port seeded with NO

Fig. 10 Lateral view of NO-PLIF images (normalized intensity) at $x = 0$ mm ($x/d^* = 0$) with upstream-torch port injection.

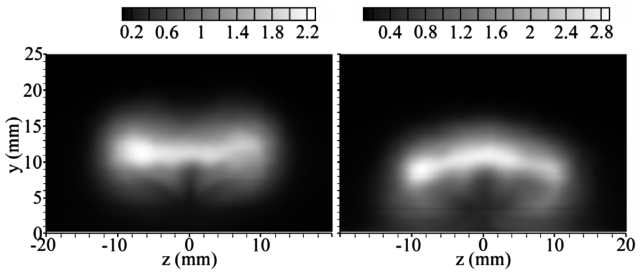

a) Single-port torch, diamond port seeded with NO

b) Dual-port torch, diamond port seeded with NO

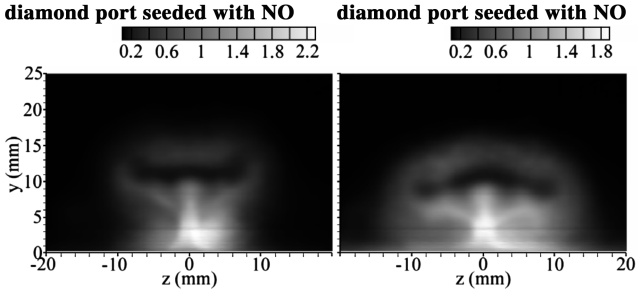

c) Single-port torch, torch port seeded with NO

d) Dual-port torch, torch port seeded with NO

Fig. 11 Lateral view of NO-PLIF images (normalized intensity) at $x = 11.4$ mm ($x/d^* = 2.17$) with upstream-torch port injection.

oblique flow behind the barrel shock in Fig. 7e was also noticeable in Figs. 9c and 9d. The region between the oblique flow and the barrel shock corresponds to the LCVP, and the torch gas was found to be entrained into this region. This suggests that the correct ER in the LCVP could be achieved by tailoring the torch-gas composition. The single-port torch case resulted in a higher penetration of the barrel shock, and thus a very small amount of the torch gas was observed to flow over the upper edge of the barrel shock.

The lateral views at $x = 0$ mm ($x/d^* = 0$) for the combined upstream-torch and main diamond injection are shown in Fig. 10. In Figs. 10a and 10b, the main injector was seeded with NO, whereas in Figs. 10c and 10d, the torch flow was seeded with NO. In this view, it was seen that the different torch arrangements produced significant changes to the overall barrel shock structure. For the single-port torch, the main-injector gas appears to penetrate more than was observed in Fig. 6a. The apparent increase in penetration was likely the result of the shielding effect the torch had on the main injector. However, the V-shaped shock still appears to be intact. The barrel shock and plume for the dual-port torch case appear to be very similar to that in Fig. 6a. The notable differences are the higher penetration and the presence of the crescent-shaped injector-gas region on the upper side of the plume. In Figs. 10c and 10d, the shape of the barrel shock was clearly visualized as the shadow region surrounded by relatively high levels of NO. The dual-port torch produced a more uniform distribution of gas around the barrel shock region. The presence of the torch gas over the upper edge of the barrel shock suggests that the torch gas is entrained into the shear layer between the freestream and the main-injector gas, which has implications for flame holding.

The lateral plane images for the two downstream measurement locations are presented in Figs. 11 and 12. From a comparison of the injector-gas trajectory (Fig. 11a) with that of the no-torch case (Fig. 6c), it was determined that the single-port torch significantly altered the flow structure at this location. Conversely, comparing the corresponding Fig. 11b, it was found that the distribution for the dual-port torch was very similar to the no-torch results. In both cases, however, the primary injector gas appeared as an elongated structure. The region below this injector gas seemed to be filled primarily with air from the freestream (or torch gas in this study), as shown in [18]. The flow visualizations with the torch gas seeded (Figs. 11c and 11d) provided a better understanding of the content in this region. The bright regions in Figs. 11a and 11b roughly align with the similarly shaped dark region in Figs. 11c and 11d, respectively. As indicated,

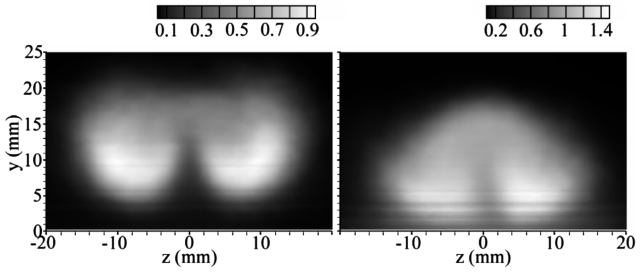

a) Single-port torch, diamond port seeded with NO

b) Dual-port torch, diamond port seeded with NO

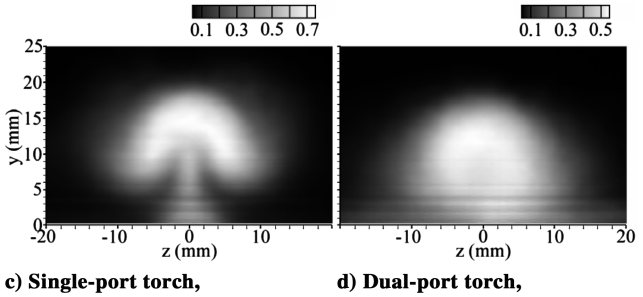

c) Single-port torch, torch port seeded with NO

d) Dual-port torch, torch port seeded with NO

Fig. 12 Lateral view of NO-PLIF images (normalized intensity) at $x = 45.7$ mm ($x/d^* = 8.70$) with upstream-torch port injection.

the torch-flow trajectories are notably different for the two cases. In both cases, there appears to be a region of high concentration along the tunnel centerline, which was expected to be the LCVP, as shown in the previous section, suggesting that the both torch configurations did not disrupt the LCVP. It should be noted that the single-port torch resulted in a taller LCVP than that of the dual-port torch case, due to the higher penetration of the barrel shock.

The single-port torch flow significantly altered the primary-injectant plume at $x = 45.7$ mm ($x/d^* = 8.70$), as evidenced by the comparison of the no-torch case in Fig. 6e with Fig. 12a. However, the dual-port torch plume (Fig. 12b) was similar to the no-torch case. The single-port torch (Fig. 12a) produced a wider plume with two very distinct lobes. This indicates that the axial counter-rotating vortex pair for the single-port torch was more dominant than for the

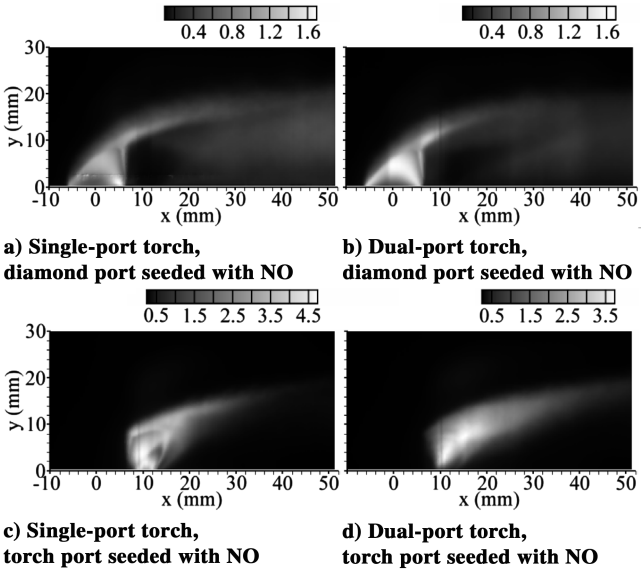

Fig. 13 Side view of NO-PLIF images (normalized intensity) with downstream-torch port injection.

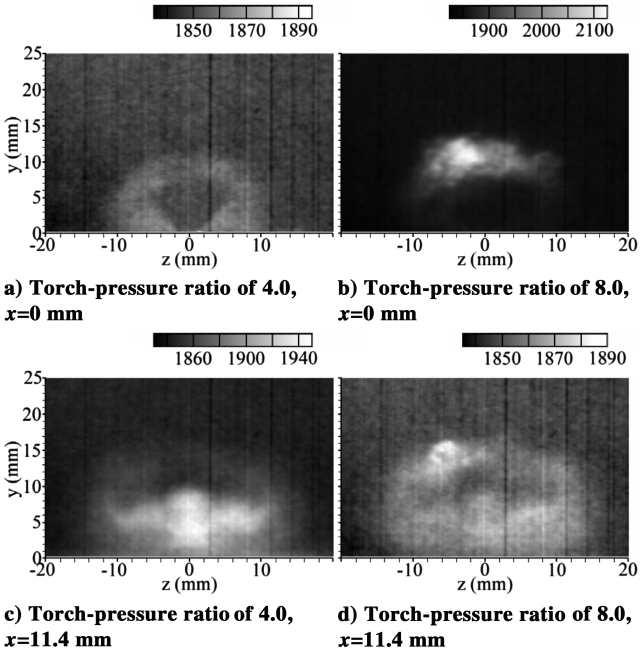

Fig. 14 Lateral view of OH-PLIF images (intensity) with the upstream dual-port torch.

other two cases. Moreover, referring to Fig. 12c, the plume shape suggests a stronger axial vortex pair than for the dual-port torch flow (Fig. 12d).

4. Downstream-Torch Case

In this study, we also examined placing the torch injectors downstream of the main injector. The purpose for these tests was to attempt to introduce the combustion products directly into the LCVP region of the flow without modifying the main-injector-barrel shock. Side-view images for these cases are shown in Fig. 13. The most notable modification to the flow for both cases was that the main-injector gas from the diamond injector was pushed further out into the freestream by torch gas than that in the no-torch case (Fig. 5b). In other words, the penetration of main-injector gas was deeper with the downstream torch than with the no-torch case. The barrel shock appeared to be unaffected by the presence of the torch-port flows. However, it appears that the wake region was filled with the torch gas. Thus, it was concluded that the LCVP would not be present for this arrangement. The barrel shock of the torch-gas plume was clearly observed in Fig. 13c, because the measurement plane cut the torch plume in this case.

B. Combustion Studies Using OH-PLIF Diagnostics

The influence of igniter-gas combustion on the upstream dual-port torch-flow characteristics were examined using OH-PLIF. This configuration choice was based on the results from the previous section, in which the dual-port torch had the smallest effect on the overall flow structure when compared with the no-torch case. The pressure ratio for the diamond injector was fixed at 10.0, and for the torch, two values of 4.0 and 8.0 were examined. As mentioned in Sec. II.A, the ethylene/oxygen torch ER was set to 2.0. For these tests, ethylene was injected from the diamond injector; the pressure ratio of 10.0 and discharge coefficient of 0.91 resulted in a bulk ER of 0.077 in the test section. The mass flow rate of the torch gas corresponded to 3.5 and 7.0% of the diamond-injector mass flow rate for the pressure ratios of 4.0 and 8.0, respectively.

Presented in Fig. 14 are the OH-PLIF results for the upstream dual-port torch configuration operating at a pressure ratio of 4.0 and 8.0. Figures 14a and 14c have the same pressure ratio as the corresponding nonreacting images in Figs. 10d and 11d. Comparison of these images at $x = 0$ mm ($x/d^* = 0$) (Figs. 10d and 14a) shows that the shapes of the barrel shock were very similar, suggesting that the combustion heat from the torch gas did not affect the shape of the barrel shock. Maintaining the shock shape is important for the formation of the LCVP. One of the reasons for this result was that the torch-gas flow rate was small compared with the injector mass flow. Also, the fuel-rich torch combustion products did not react with the freestream to a significant level around the barrel shock. This was clearly determined, because the OH and NO torch-gas distributions were very similar, though the OH fluorescence was very weak. If further reactions had occurred, it is expected that the OH region in Fig. 14a would have been noticeably wider than the corresponding NO region in Fig. 10d, due to additional generation of OH during the reactions. At $x = 11.4$ mm ($x/d^* = 2.17$), the NO-PLIF measurements (Fig. 11d) showed an accumulation of torch gas in the LCVP region. For the ethylene experiments using OH-PLIF (Fig. 14c), this region was slightly larger than that in the corresponding NO-PLIF image, showing that an additional reaction may have occurred in the LCVP region. However, the OH fluorescence was very weak. Thus, if additional combustion occurred, it was not extensive.

The higher-torch-pressure case (Fig. 14b) showed a feature not present in the low-pressure case. Specifically, an accumulation of OH was observed over the upper edge of the barrel shock, and a bright spot was seen in the region. The OH on the both sides of the barrel shock was hidden due to the grayscale range being shifted to show the details of the bright spot. It should also be noted that OH fluorescence was still very weak. Nonetheless, the bright spot suggests additional combustion around the barrel shock. The downstream image for the high-pressure case (Fig. 14d) also has a bright spot, which seemed to originate from the bright spot in the former image. However, the downstream spot was smaller, which indicated that the combustion was undergoing extinction. Entrainment of OH into the LCVP region was also observed for this high-torch-pressure case. Intense combustion was not observed in this region.

For the present set of combustion tests, the lack of intense combustion in the LCVP was not surprising, because the pressure in the LCVP region was relatively low (the wind-tunnel freestream static pressure was 26 kPa) and no attempt was made to actively control the ER in this region. As suggested by the numerical simulations, the mixture in the LCVP was expected to be extremely fuel-rich, and thus the fuel-rich torch did not promote the reaction in this region. Note, however, that the temperature in the LCVP region is relatively high (near the stagnation temperature), which, from an Arrhenius reaction rate perspective, is more important than pressure. The next step for improvement is to develop a method to control the fuel concentration to sustain a flammable mixture in the LCVP.

IV. Conclusions

A series of mixing and combustion tests using a diamond-shaped fuel injector was conducted in a Mach 2.0 freestream. The goals were to 1) examine the flow structure in the near-field region of the diamond- and circular-port injectors using advanced laser diagnostics and 2) quantify the effects of igniter-torch flow on the near-field flow structure with and without torch gas.

NO- and OH-PLIF diagnostics were used to examine the flow structure and combustion potential, respectively. The specific findings are summarized as follows. First, the tailored flow structure predicted in [6] for the 15-deg half-angle diamond injector operating at a pressure ratio of 10 was verified with the NO-PLIF images. Specifically, the predicted necessary modifications to the barrel shock were observed. Second, it was determined from the NO-seeded-air studies that the upstream dual-port torch flow had the least impact on the diamond-injector flow structure and the most uniform distribution of the torch gas (around the perimeter of the main-injector gas). Third, the accumulation of NO-seeded upstream-torch gas in the LCVP region provided additional evidence for the presence of a trapped vortex pair in this region. Fourth, the diamond injector produced a larger and more diffuse downstream plume (which suggested improved mixing) than that with the circular injector. Fifth, the combined single-port torch and diamond injector produced the best far-field spreading of the main-injector flow. Sixth, the OH-PLIF results from the operating torch igniter were very similar to those from the nonreacting NO-PLIF, which indicated that the heat release due to the torch gas did not significantly alter the tailored injector flow.

Acknowledgments

The authors would like to acknowledge the contributions of W. Seward and C. Adcock (Texas A&M University) and D. Schommer, W. Terry, T. Barhorst, C. Smith, and K. Kirkendall (Innovative Scientific Solutions, Inc.) for their technical support of this work. The support of the Research Air Facility of the U.S. Air Force Research Laboratory is also appreciated.

References

[1] Hieser, W., and Pratt, D., *Hypersonic Airbreathing Propulsion*, AIAA Education Series, AIAA, Washington D.C., 1994.

[2] Schetz, J., Thomas, R., and Billig, F., "Mixing of Transverse Jets and Wall Jets in Supersonic Flow," *Separated Flows and Jets*, edited by V. V. Koslow and A. V. Dovgal, Springer–Verlag, Berlin, 1991, pp. 807–837.

[3] Barber, M., Schetz, J., and Roe, L., "Normal Sonic Helium Injection Through a Wedge-Shaped Orifice into a Supersonic Flow," *Journal of Propulsion and Power*, Vol. 13, No. 2, 1997, pp. 257–263.

[4] Tomioka, S., Jacobsen, L., and Schetz, J., "Sonic Injection from Diamond-Shaped Orifices into a Supersonic Crossflow," *Journal of Propulsion and Power*, Vol. 19, No. 1, 2003, pp. 104–114.

[5] Bowersox, R., Fan, H., and Lee, D., "Sonic Injection into a Mach 5.0 Freestream Through Diamond Orifices," *Journal of Propulsion and Power*, Vol. 20, No. 2, 2004, pp. 280–287.

[6] Srinivasan, R., and Bowersox, R., "Simulation of Transverse Gaseous Injection Through a Diamond Port into a Supersonic Freestream," *Journal of Propulsion and Power* (to be published).

[7] Davis, D., and Bowersox, R., "Computational Fluid Dynamics Analysis of Cavity Flame Holders for Scramjets," 33rd AIAA/ASME/SAE/ASEE Joint Propulsion Conference, Seattle, WA, AIAA Paper 97-3270, 1997.

[8] Kobayashi, K., Tomioka, S., and Mitani, T., "Supersonic Flow Ignition by Plasma Torch and H_2/O_2 Torch," *Journal of Propulsion and Power*, Vol. 20, No. 2, 2004, pp. 294–301.

[9] Gruber, M., and Nejad, A., "New Supersonic Combustion Research Facility," *Journal of Propulsion and Power*, Vol. 11, No. 5, 1995, pp. 1080–1083.

[10] Kobayashi, K., Kanda, T., Tomioka, S., Tani, K., Sakuranaka, N., and Mitani, T., "Suppression of Combustor-Inlet Interaction in a Scramjet Engine Under Mach 4 Flight Conditions," *Transactions of the Japan Society for Aeronautical and Space Sciences*, Vol. 49, No. 166, 2007, pp. 246–253.

[11] Kobayashi, K., Tomioka, S., and Mitani, T., "H_2/O_2 Torch Igniter for Scramjet Engine Tests," International Symposium on Space Technology and Science Paper 2004-a-29, Jun. 2004.

[12] Radhakrishnan, K., "LSENS—A General Chemical Kinetics and Sensitivity Analysis Code for Homogeneous Gas-Phase Reactions," NASA RP-1328, 1994.

[13] GASP, Software Package, Ver. 4.0, AeroSoft, Inc., Blacksburg, VA, 2001.

[14] Roe, L., "Approximate Riemann Solvers, Parameter Vector, and Difference Schemes," *Journal of Computational Physics*, Vol. 43, No. 2, 1981, pp. 357–372.

[15] Harten, A., and Hyman, J., "Self Adjusting Grid Methods for One-Dimensional Hyperbolic Conservation Laws," *Journal of Computational Physics*, Vol. 50, No. 2, 1983, pp. 235–269.

[16] Wilcox, D., *Turbulence Modeling for CFD*, DCW Industries, Inc., La Canada, CA, 1998.

[17] Srinivasan, R., and Bowersox, R., "Detached-Eddy Simulation of Gaseous Injection into a Mach 5.0 Freestream," *AIAA Journal* (submitted for publication); also 43rd AIAA Aerospace Sciences Meeting, Reno, NV, AIAA Paper 2005-0894, 2005.

[18] Gruber, M., Nejad, A., Chen, T., and Dutton, J., "Transverse Injection from Circular and Elliptic Nozzles into a Supersonic Crossflow," *Journal of Propulsion and Power*, Vol. 16, No. 3, 2000, pp. 449–457.

J. Oefelein
Associate Editor